Accelerating 3D single-molecule localization microscopy using blind sparse inpainting

Sunil Kumar Gaire[1], Hao F. Zhang[2], and Leslie Ying[1,3*]

[1]Department of Electrical Engineering, The State University of New York at Buffalo, Buffalo, NY, 14260, USA
[2]Department of Biomedical Engineering, Northwestern University, Evanston, IL, 60208, USA
[3]Department of Biomedical Engineering, The State University of New York at Buffalo, Buffalo, NY, 14260, USA
[*]leiying@buffalo.edu

ABSTRACT

Single-molecule localization-based super-resolution microscopy has enabled the imaging of microscopic objects beyond the diffraction limit. However, this technique is limited by the requirements of imaging an extremely large number of frames of biological samples to generate a super-resolution image, thus requires longer acquisition time. Additionally, processing of such a large image sequence leads to longer data processing time. Here, we present a computational algorithm to accelerate 3D single-molecule localization microscopy (SMLM) technique by using blind sparse inpainting. This technique reconstructs the high-density 3D images from low-density ones, without compromising the resolution. The low-density images are generated using much fewer frames than usually needed by the high-density images, thus requiring shorter acquisition and processing time. Thus, the algorithm will accelerate 3D SMLM without changing the existing SMLM hardware system. Superior reconstruction results of 3D SMLM images are presented using up to 10-fold fewer frames in simulation data and up to 50-fold fewer frames in experimental data.

Introduction

Single-molecule localization microscopy (SMLM) such as (direct) stochastic optical reconstruction microscopy ((d)STORM)[1,2], (fluorescence) photoactivated localization microscopy ((f)PALM)[3,4], and other variants[5–8] have extended the imaging resolution of conventional optical fluorescence microscopy beyond the diffraction limit (~ 250 nm). In these methods, a sparse subset of fluorophores in the sample is imaged in each diffraction-limited image frame, whereas a large number of such frames are obtained sequentially. Then the detected individual fluorophores in each frame are precisely localized, and finally all the localization positions from these frames are assembled together to generate the super-resolution image. 3D SMLM[9–12] requires additional axial (z-axis) information, which is obtained by using z-dependent point spread functions (PSFs)[13]. Optically engineered PSFs such as astigmatic[9], double-helix[14], bi-plane[15], interferometric based[16], and airy-beam based[17] PSFs are commonly used in existing 3D SMLM imaging to encode the axial information of blinking fluorescent molecules. In both 2D and 3D SMLM imaging, to achieve sufficient dense localizations to reveal details of biological samples, a large number of sequential diffraction-limited frames (typically $> 10^4$) are needed, suggesting long acquisition time. This also makes potential live-cell and high-throughput imaging more challenging. Practically, the acquisition of such long frame sequences also results in the degradation of image quality due to photobleaching of the dyes. Furthermore, the processing of such a large number of frames requires considerable processing times[18]. Several approaches have been explored to accelerate imaging speed. One of them was to apply fast switching rates for fluorophores (probes), but such techniques of increasing switching rates may cause photobleaching of the probes and thus image quality degradation[10]. Another approach was to increase the number of active fluorophores per frames[19,20]. However, the high density causes fluorescent spots to overlap in the diffraction-limited images, making it more difficult to localize the fluorophores precisely[20]. Despite these challenges, most of the existing techniques[21–23] use higher molecular density per frame to increase the imaging speed.

Here, we present a computational approach to accelerate 3D SMLM imaging. The experimental setup and data acquisition procedure remain the same as those of standard 3D SMLM methods, except that very few diffraction-limited frames are acquired, which will reduce the acquisition time and ultimately accelerate imaging speed. Further, the data processing time will also be reduced accordingly. For the standard 3D SMLM methods, the final image rendered from very few frames is sparse and provides less information to extract the fine structures of the biological sample. Our method is capable of recovering those unresolved structures in the sparse image and reconstructing the high-quality 3D super-resolution image. The fast 2D SMLM imaging using the blind sparse inpainting has been previously reported in detail[24]. Here, we extended it to accelerate 3D SMLM imaging by introducing a new sparsifying transform appropriate for the 3D structure. In our previous work, high-

density 2D SMLM images were reconstructed by solving an l_1 minimization problem using the alternating direction method of multipliers (ADMM)[25] with curvelet transform[26] as the sparsifying transform. Here, we also use ADMM but with combined curvelet transform and an additional total variation (TV) for the depth direction. We confirm the efficacy of the proposed algorithm using both simulated and experimental 3D SMLM data sets. The preliminary results of this paper were reported in[27]. This expanded report includes additional simulation and quantitative evaluation results, as well as experimental results.

Results

Reconstruction approach

In standard 3D SMLM, a large number of diffraction-limited frames (suppose N frames) are imaged with a total acquisition time of $N\Delta t$, where Δt is the time to acquire a single frame (typically 10-30 ms), and processed to produce a high-density 3D super-resolution image. A smaller number of frames (suppose Q frames and $Q << N$) with a shorter acquisition time of $Q\Delta t$ render a low-density 3D image (Fig. 1). Our goal is to reconstruct the high-density 3D image using a low-density 3D image acquired using fewer frames, which is sparse and incomplete. To reconstruct the high-density 3D image, we need to restore the unknown fluorophore localization points based on the available fluorophore localization points on the low-density 3D image. Thus, the restoration problem can be formulated as an image inpainting task, which aims to restore the missing regions of the corrupted image and reconstruct the original image[24]. Mathematically, the relationship between the low-density 3D image x_Q composed of the localized points acquired in Q frames and the desired high-density 3D image x can be modeled as

$$\mathbf{x}_Q = \mathbf{P}_Q \mathbf{x}, \tag{1}$$

where P_Q is a diagonal matrix with either element 1 for the acquired location or 0 for the missing location. To solve (1), we first estimate the unknown measurement matrix P_Q (called "blind") based on the low-density 3D image and then reconstruct x from x_Q. The estimation of P_Q is challenging in the sense that zero-valued pixel in x_Q can be background without any fluorophore or those with fluorophore but not detected in the acquired Q frames. By performing hard-thresholding on the low-density image, the locations of fluorescence molecules captured in Q frames are determined.

After P_Q is obtained, x can be estimated from x_Q, which is still non-trivial because of infinite possible solutions. Here, we reconstruct the desired high-density 3D image by enforcing sparseness. Specifically, the high-density 3D image is reconstructed by solving the following unconstrained minimization problem:

$$\min_x \quad \lambda_1 \left\| \mathbf{P}_Q \mathbf{x} - \mathbf{x}_Q \right\|_2^2 + \left\| \mathbf{\Phi x} \right\|_1 + \lambda_2 \mathrm{TV}(\mathbf{x}) , \tag{2}$$

where $\|.\|_1$ and $\|.\|_2$ represent the l_1 and l_2 norm respectively, λ_1 and λ_2 are weight parameter and regularization parameter, respectively, Φ represents a sparsifying transform, and $\mathrm{TV}(\cdot)$ is a total variation regularization. The first term enforces data consistency, the second term enforces the sparsity in the transform domain, and the third term promotes the piecewise smoothness of the image. Many biological structures, such

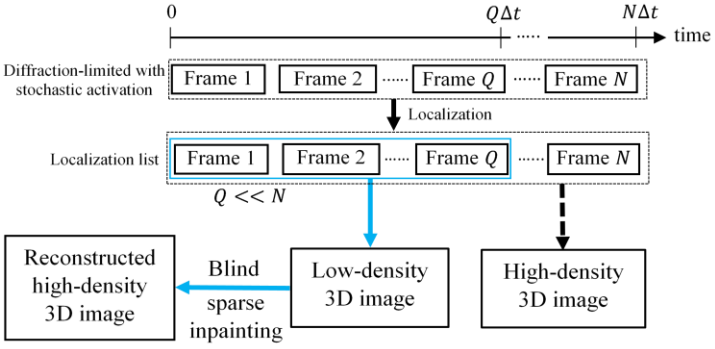

Figure 1. Comparison of blind sparse inpainting method with the existing 3D SMLM method. 3D super-resolution image in existing SMLM is obtained by imaging and processing a large number of diffraction-limited single-molecule frames (suppose N frames). The proposed method uses very few diffraction-limited frames (suppose Q frames and $Q << N$). The high-density 3D image is reconstructed using blind sparse inpainting from the low-density 3D image obtained from Q frames.

as microtubules, are of anisotropic curve-like nature. Therefore, we use the curvelet transform as a sparsifying transform in the lateral plane. It provides sparsity as well as excellent directional sensitivity and anisotropy. Thus, it can efficiently characterize anisotropic features such as edges, arcs, and curves[28]. The discrete curvelet transform (DCT) was implemented using *CurveLab*[29] with curvelets via the wrapping approach. It includes four steps: 2D FFT (fast Fourier transform), windowing, frequency wrapping, and 2D inverse FFT[26]. TV regularization is used in the depth direction only, where TV is defined as $TV(\mathbf{x})=\|\mathbf{Gx}\|_1$, where $\boldsymbol{G}$ is the first-order finite-difference operator along the depth direction, and $\|\cdot\|_1$ denotes the L1 norm. More detail about the optimization algorithm is in the Methods section. All the parameters in our implementation were tuned heuristically, and the best results obtained from the quantitative evaluations are presented.

Simulation results

To evaluate the performance of our method, we generated a simulated 3D SMLM image in the shape of a knot as the "ground-truth" specimen (Supplementary movie 1). The phantom knot had a volume of dimension 4.02 µm × 4.02 µm × 0.18 µm with the lateral and axial resolution of ~ 20 nm and ~ 17 nm, respectively (Fig. 2(e,i)). The localization list was simulated by

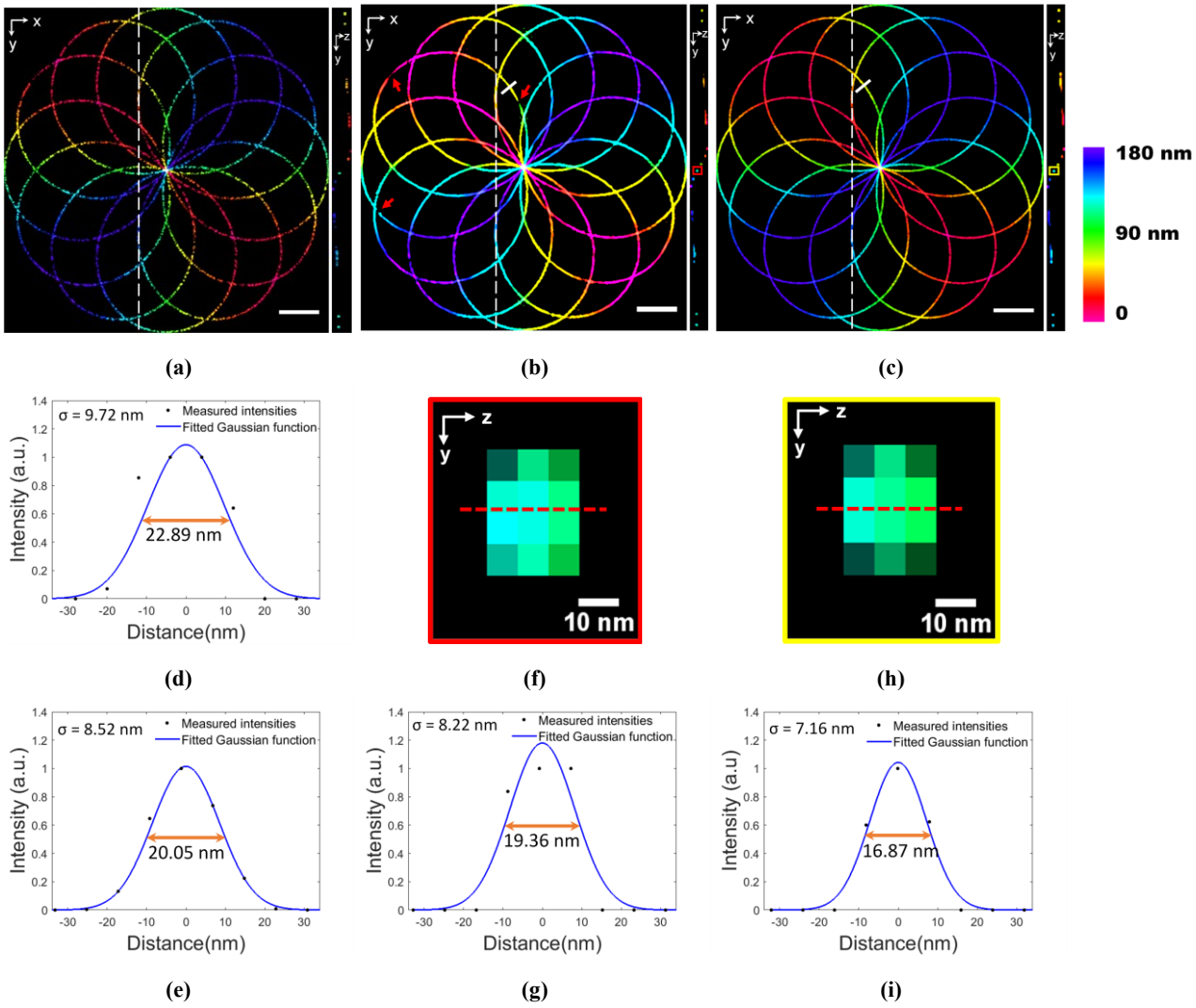

Figure 2. Blind sparse inpainting reconstruction of simulated 3D SMLM image. (a-c) Low-density image using 1000 frames, blind inpainting reconstruction, and high-density ground-truth image using 10,000 frames, respectively. The right panel in each image show (y,z) slice at the position indicated by the white dashed line. The color-bar shows the depth of *z*. Scale bars: 0.5 µm. Pixel Size: 8 nm. (d,e) Intensity profile and FWHM at the white line segment shown in the reconstructed image (b) and the reference image (c), respectively. (f) Zoomed in view of red rectangular box in (y,z) slice of (b). (g) Intensity profile and FWHM along the red dotted line segment in (f). (h) Zoomed in view of yellow rectangular box in (y,z) slice of (c). (i) Intensity profile and FWHM of the red dotted line segment in (h).

randomly selecting some locations in the knot as the activated fluorophores molecules with an activation density of approximately 10 molecules per frame[12] (3.44 molecules/μm^3 per frame). The localized coordinates (x,y,z) and intensities of the activated molecules were then recorded for each camera frame. Since the localization points were directly obtained from the true image (assuming obtained from localization algorithms), there were no localization errors or background noise. Each location in the list, which describes the fluorescent molecule at that point, was then used to obtain the 3D image. The increasing density of the generated images can be synthesized by combining the localization points from more frames. We used fewer frames to generate the low-density 3D image and then apply our blind sparse inpainting algorithm to reconstruct the high-density 3D image.

To reconstruct the 3D high-density image from the low-density image, we constructed 22 z-slices of the low-density 3D image by grouping the localization data in z-axis with a thickness of 8 nm, i.e., Δz= 8 nm. ThunderSTORM[30], an open-source SMLM data analysis plugin for Fiji[31], was used to computationally render these z-slices using average shifted histogram method[32] as a method of visualization, with the simulated localization list as an input. The result in Fig. 2b shows that the blind sparse inpainting reconstruction of the low-density image rendered with Q=1000 frames and 15,910 localization points significantly improves the localization density, and is visually equivalent to the ground-truth image rendered with N=10,000 camera frames and 96,203 fluorophore localization points (Fig. 2c). The 3D projection of Fig. 2(a-c) is shown in supplementary movie 2. Additionally, the volume visualization of the simulated low-density, blind-inpainting reconstruction, and ground-truth 3D images using the Volume Viewer[33] plugin in Fiji is shown in Fig. 3. Most of the incomplete and rough curvilinear structures due to reduced localization points in the low-density image are reconstructed almost perfectly, giving complete and continuous filament structures with an excellent agreement with the ground-truth image. At some positions, where the input low-density image has very little information available, the reconstruction still deviates from the ground truth (red arrows in Figs. 2b & 3b). Such errors can be reduced by increasing the frame numbers (thereby the number of localization points) but at the cost of reduced acceleration.

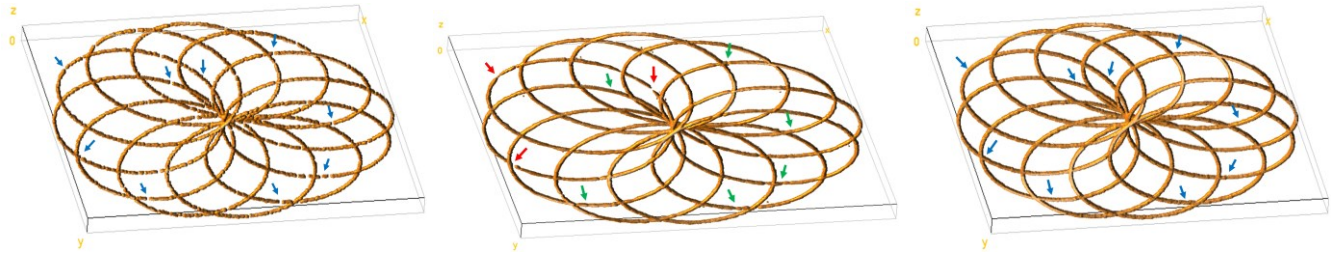

(a) **(b)** **(c)**

Figure 3. Volume visualization of the simulated 3D image. (a-c) Low-density, reconstructed, and ground-truth 3D images, respectively. Green arrows in (b) show proper reconstructions. At some positions, the blind sparse inpainting failed to give superior reconstruction, as shown by red arrows. The low-density image was rendered using 1000 frames, and the ground-truth image was obtained using 10,000 frames.

The resolution of the reconstructed image was evaluated using the full width at half maximum (FWHM) of the intensity profile along the lateral and axial directions, as shown in Figs. 2(d) and 2(g), respectively. The black dots are measured intensities, and the blue curves are fitted Gaussian functions, with standard deviation σ and FWHM (double orange arrow) as indicated. The FWHM values were calculated using FWHM = $2\sqrt{2ln2}\,\sigma \approx 2.355\sigma$. The FWHM values of the reconstructed image in both lateral and axial directions are similar (≈ 2.5 nm higher) to those of the ground-truth image (Fig. 2(e,i)), indicating the inpainted reconstruction is able to preserve the resolution of 3D structure.

For the quantitative evaluation of the reconstruction, we calculated the true positive rate (TPR), false-positive rate (FPR), and root mean squared error (RMSE) of the reconstructed image by comparing it with the ground-truth. TPR was defined as a ratio of the number of correctly recovered non-zero pixels in the foreground region of the reconstructed image versus the total number of those present in the ground-truth. A higher value of TPR indicates fewer missed non-zero pixels in the foreground region. FPR was defined as a ratio between the falsely recovered non-zero pixels that belong to the background region, and the total number of those present in the ground-truth. A higher value of FPR indicates more incorrect locations, whereas a lower FPR ensures proper reconstructions. Since the generation of the localization list is random, we conducted ten simulations and calculated the average TPR and FPR for different numbers of frames, as shown in Fig. 4(a,b). The TPR improves with the increasing number of frames, while the FPR is lower than 0.5% over the entire range in the simulation. The reconstructed image of Fig. 2 using 1000 frames had a TPR of about 80% and a FPR of 0.10%. Furthermore, we calculated

the RMSE between the reconstruction images and the ground truth image (Fig. 4c). The RMSE result is also an average of ten simulations. The curve shows significant improvements in the reconstruction with greater than 800 frames. The RMSE value for blind sparse inpainting reconstruction of Fig. 2 using 1000 frames was 0.0748.

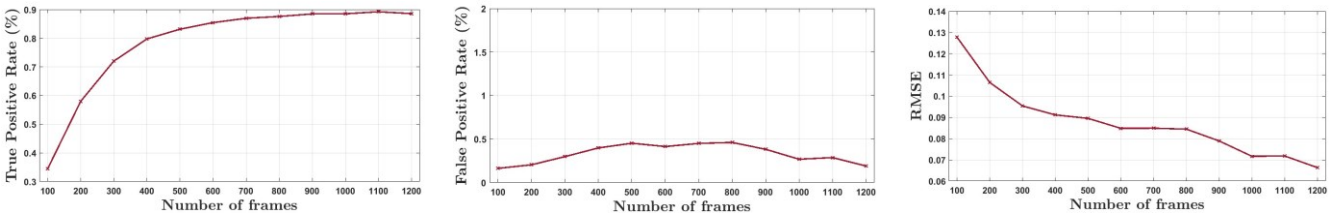

(a) **(b)** **(c)**

Figure 4. Quantitative evaluation of simulation results. (a-c) True positive rates, False positive rates, and RMSE, respectively, for the different number of frames.

Experimental results

To demonstrate the performance of blind sparse inpainting reconstruction for real 3D SMLM image, we used two sets of localization list of experimental microtubules data that are publicly available.

The first data set was from the Ecole Polytechnique Fédérale de Lausanne (EPFL) 3D SMLM software challenge [34]. The details about sample preparation and microscopy setup can be found in[35]. In brief, microtubules in U-2 OS cells were labeled with anti-alpha tubulin primary and Alexa Fluor 647-coupled secondary antibodies. The diffraction-limited frames were imaged using the optical setup of dSTORM[1] with a cylindrical lens. We used the wobble and drift corrected "Tubulin-A647-3D" localization list results obtained from 112,683 frames processed using ThunderSTORM. When all 112,683 frames with about 7.4 million of localization points were used, we obtained a high-density super-resolution 3D image, which was used as a reference image (Fig. 5c). The low-density image was synthesized using 2,254 frames, i.e., 50 fold fewer frames, with about 0.1 million of localization points from the same localization list data (Fig. 5a). To reconstruct the 3D high-density image from the low-density image, we constructed 23 z-slices of the low-density 3D image with FoV of 37.1 µm × 33.44 µm by grouping the localization list data in z-axis with a size of 50 nm, i.e., Δz= 50 nm. The overall axial range was 1,150 nm. The microtubule filaments can already be seen in the low-density image, but structural details were hard to discern. To reconstruct the high-density 3D image, our blind sparse inpainting algorithm was applied to the low-density 3D image. The colorized low-density, reconstructed, and reference 3D images with color indicating the depth in the z-direction are shown in Fig. 5(a-c), respectively. Visual observation shows that blind sparse inpainting reconstruction significantly improves the localization density as compared to the low-density image. A slice of the 3D images is also presented in Fig. 5(d-f). The microtubule's filament structures are more clearly revealed in the reconstruction slice (Fig. 5e) with much denser localization points compared to the low-density slice (Fig. 5d).

For the quantitative evaluation of the reconstructed images of experimental data, we used multiscale structural similarity index (MS-SSIM)[36], a perceptually motivated metric, between the reference high-density image and the reconstructed image. Since the ground truth is not available for the experimental data, the high-density 3D images rendered with all available frames were used as reference images. Also, it is worth noting that this reference high-density image still might deviate from the ground truth. So, the RMSE with reference image is not a proper metric for quantitative evaluation of reconstruction as the pixel value difference can be large even for perfect reconstruction[24]. Thus, we used MS-SSIM to evaluate the capability of reconstruction to capture the structural information in the reference image of experimental data sets. The MS-SSIM index has a scale between 0 and 1, with 1 being a perfect match with the reference image. The higher MS-SSIM value indicates a better match of structural information. Fig. 6 shows the improvement in the MS-SSIM index of the reconstructed 3D image slices compared to that of the input low-density 3D image slices. It demonstrates that our method is capable of recovering the structures of microtubules with high similarities with the reference high-density image. The MS-SSIM index of the edge slices (slices 1, 22, and 23) are still low because of having very low localization densities with a wide gap between the fluorophore localization in those slices.

To further evaluate the blind sparse inpainting reconstruction for 3D SMLM experimental data, we used another publicly available microtubule localization list result obtained from ZOLA-3D (Zernike Optimized Localization Approach in 3D)[37]. Details about sample preparation, imaging setup, and processing steps can be found in[11]. In brief, microtubules in a U-373 MG cell was labeled with anti-alpha tubulin primary and Alexa-647 conjugated secondary antibodies. The 3D image was then

acquired with the saddle point PSF using water immersion optics and using a total of 87,949 frames. High-density 3D super-resolution image was generated using all 87,949 frames with around 957,000 localization points, visualizing the whole cell with an axial range of 2.2 µm (Fig. 7c). The low-density 3D image was generated using 1,750 frames, i.e., 50 fold fewer frames, with approximately 22,800 localization points from the same localization data (Fig. 7a). For reconstruction, we constructed 22 *z*-slices of the low-density image by grouping the localization data in *z*-axis with a size of 100 nm, i.e., Δz= 100 nm with an FoV of 51.2 µm × 42.4 µm.

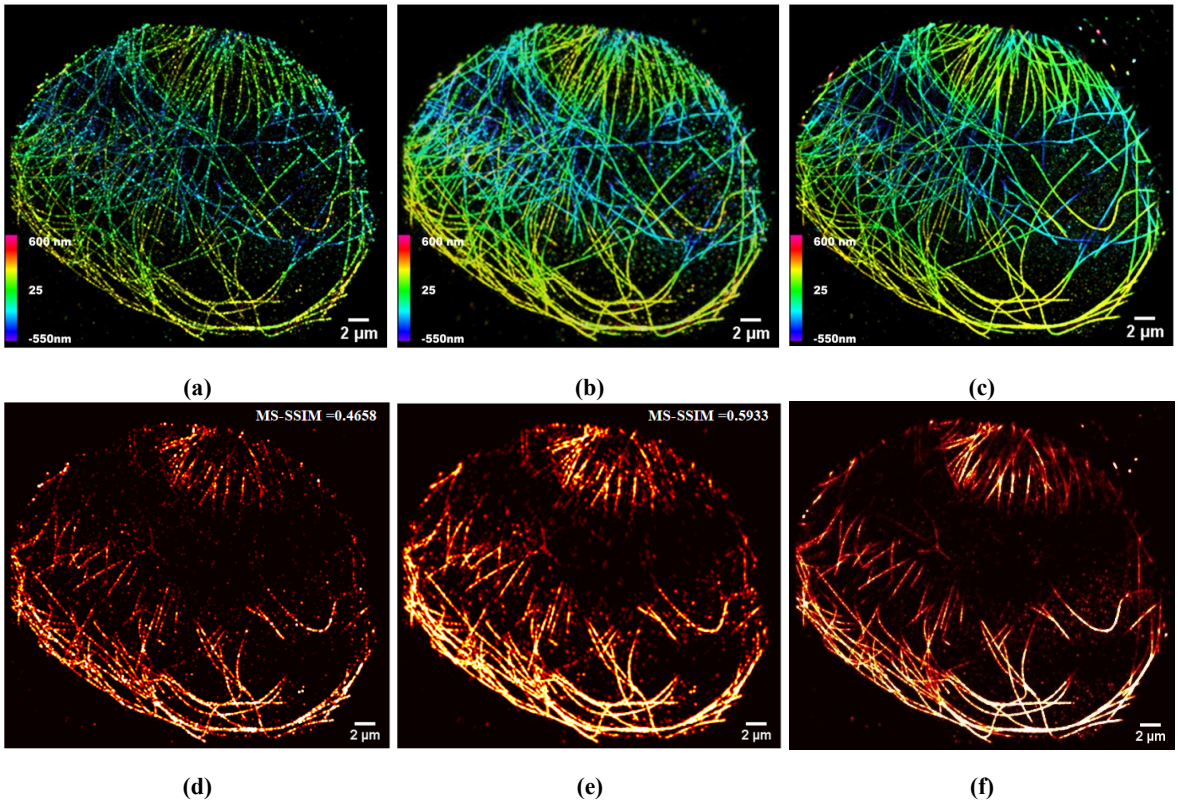

Figure 5. Blind sparse inpainting reconstruction results of "Tubulin-A647-3D" data. (a-c) The low-density, reconstructed, and high-density super-resolution 3D image with color indicating the depth of *z*. The low-density image was rendered using 2,254 frames, and the high-density image was obtained using 112,680 frames. (d-f) The low-density, blind sparse inpainting reconstruction and high-density images of a slice of images (a-c), respectively, in the depth direction. Pixel Size: 80 nm.

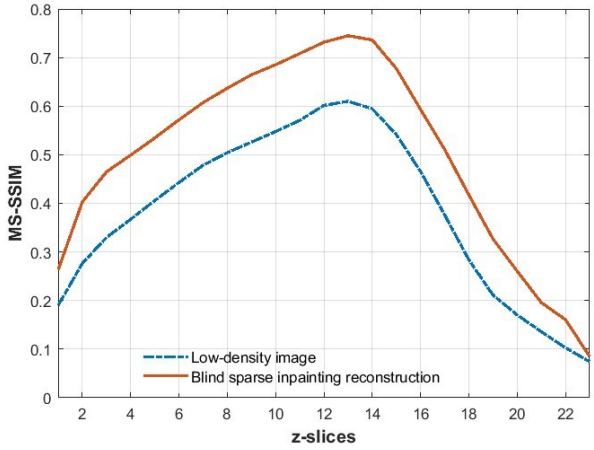

Figure 6. The plot of MS-SSIM index vs. *z*-slices for comparing the reconstruction of microtubules structures for "Tubulin-A647-3D" image. Blind sparse inpainting reconstruction showed the improved MS-SSIM for all *z*-slices.

Then, the low-density image was given as an input to our blind sparse inpainting algorithm. Colorized 3D images, with color indicating the z-axis, for low-density, reconstructed, and high-density images are shown in Figs. 7 (a-c), respectively. One z-slice of the corresponding images are also presented respectively in Figs. 7 (d-f). Microtubule structures are more clearly revealed in reconstruction with much higher localization densities, which are comparable to the reference high-density image. The improvement in the MS-SSIM index, as shown in Fig. 8, also verifies higher similarities with the high-density reference image after the reconstruction. However, some fine features in the high-density image with the dense or close-by structure were not resolved properly due to the error in the blind estimation of P_Q.

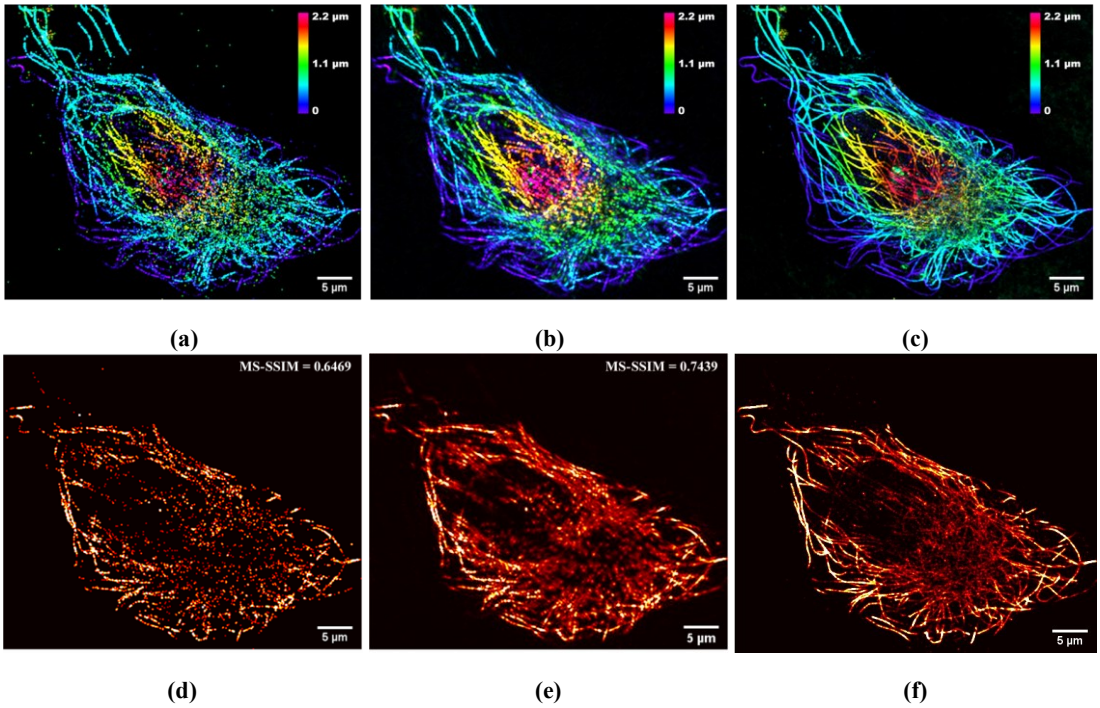

Figure 7. Blind sparse inpainting reconstruction of microtubules data from ZOLA-3D. (a-c) The low-density, reconstructed, and high-density 3D super-resolution image with color indicating the depth of z. The low-density image was obtained using 1,750 frames, and the high-density image was obtained using 87,949 frames. (d-f) The low-density, blind sparse inpainting reconstruction and high-density images of a slice of images (a-c), respectively, in the depth direction. Pixel Size: 100 nm.

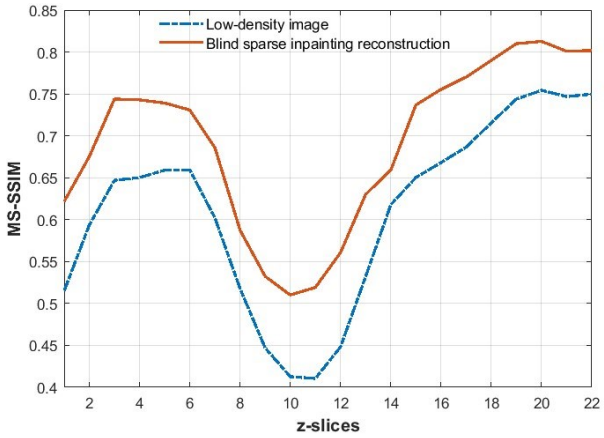

Figure 8. The plot of MS-SSIM index vs. z-slices for the ZOLA-3D data. Blind sparse inpainting reconstruction showed the improved MS-SSIM for all z-slices.

Discussion

We present a computational method based on blind sparse inpainting to reconstruct the high-density 3D super-resolution images using the low-density 3D images synthesized using very few camera frames obtained from the standard SMLM data. We showed superior reconstruction using a 10-fold reduction in the number of frames in the simulated 3D SMLM image and a 50-fold reduction in the number of frames for experimental microtubules 3D SMLM images. Thus, the acquisition time is reduced considerably by using much lower camera frames, thus accelerating the imaging speed of 3D SMLM. Also, blind inpainting reconstruction preserves the resolutions of the 3D images. Further, to accelerate the 3D SMLM imaging, no change in existing optical setup and labeling protocol is needed. We expect that by integrating with the existing higher molecular density labeling methods[21–23], our method can offer further improvement in the acquisition time. However, since missing localization points are estimated blindly, there may be some errors in predicting the P_Q, which may give some artifacts or loss of resolutions. Such limitations can be alleviated by using more frames at the cost of reduced accelerations. We anticipate that combining super-resolution optical microscopy and our blind inpainting method enables future real-time live-cell and high-throughput imaging to investigate the complex nanoscopic biological structures and their functions.

Methods

Optimization algorithm

The convex optimization problem of (2) is a standard minimization problem. It can be solved using efficient approaches such as variable splitting and augmented Lagrangian method (ALM). In this paper, we are using a specific variation of ALM called ADMM. We first introduce the auxiliary variable $\mathbf{d} = \mathbf{\Phi x}$ and $e = Gx$ in (2) to decouple the l_1 term from other parts and obtain the following equivalent form

$$\begin{aligned} &\min_{x} \quad \lambda_1 \left\| P_Q x - x_Q \right\|_2^2 + \|d\|_1 + \lambda_2 \|e\|_1 \\ &\text{s.t.} \quad \Phi x = d \quad \text{and} \quad Gx = e. \end{aligned} \tag{3}$$

The scaled form of the augmented Lagrangian function of (3) can be written as

$$L(x,d,e,u,v) = \frac{\lambda_1}{2} \left\| P_Q x - x_Q \right\|_2^2 + \|d\|_1 + \lambda_2 \|e\|_1 + \frac{\rho}{2} \|\Phi x - d + u\|_2^2 + \frac{\mu}{2} \|Gx - e + v\|_2^2 \tag{4}$$

where u and v are Lagrangian multipliers representing scaled dual variables. Similarly, ρ and μ are the penalty parameters. The ADMM iteration scheme will be

$$x^{k+1} = \underset{x}{\arg\min} \ \frac{\lambda_1}{2} \left\| P_Q x - x_Q \right\|_2^2 + \frac{\rho}{2} \|\Phi x - d^k + u^k\|_2^2 + \frac{\mu}{2} \|Gx - e^k + v^k\|_2^2 \tag{5}$$

$$d^{k+1} = \underset{d}{\arg\min} \ \|d\|_1 + \frac{\rho}{2} \|\Phi x^{k+1} - d + u^k\|_2^2 \tag{6}$$

$$e^{k+1} = \underset{e}{\arg\min} \ \lambda_2 \|e\|_1 + \frac{\mu}{2} \|Gx^{k+1} - e + v^k\|_2^2 \tag{7}$$

$$\boldsymbol{u^{k+1} = u^k + \Phi x^{k+1} - d^{k+1}} \tag{8}$$

$$v^{k+1} = v^k + Gx^{k+1} - e^{k+1} \tag{9}$$

The x- subproblem has a closed-form solution

$$\boldsymbol{x^{k+1} = B(\lambda_1 P_Q^T x_Q + \rho \Phi^H (d^k - u^k) + \mu G^H (e^k - v^k)} \tag{10}$$

where $B = (\lambda_1 P_Q^T P_Q + \rho I + \mu I)^{-1}$. The superscripts H and T denote the Hermitian transform and the transpose of a matrix, respectively. The optimum values of d-subproblem and e-subproblem are obtained through element-wise shrinkage operator

$$\boldsymbol{d^{k+1} = shrink\left(\Phi x^{k+1} + u^k, \frac{1}{\rho}\right)} \tag{11}$$

$$\boldsymbol{e^{k+1} = shrink\left(Gx^{k+1} - v^k, \frac{\lambda_2}{\mu}\right)} \tag{12}$$

where

$$shrink(x,\gamma) = \frac{x}{|x|} \max(|x| - \gamma, 0). \tag{13}$$

The algorithm terminates when the predefined maximum number of iteration is reached. The proposed ADMM optimization algorithm for blind sparse inpainting is summarized in Algorithm 1. The algorithm and analysis were implemented in MATLAB R2018a.

Algorithm 1

Input: x_Q−low density 3D image.
$\lambda_1, \lambda_2, \beta$−weight, TV regularization parameters and scalar constant.
ρ, μ−penalty parameters.
Φ− sparsifying transform operator.
n− maximum number of iterations (stopping criteria).
Output: x−high density 3D image.
Initialization: $d^0 = 0$, $e^0 = 0$, $u^0 = 0$, $v^0 = 0$, $count = 1$.
for $count = 1 : n$ **do**
Solve x−subproblem using (10).
Solve d−subproblem using (11).
Solve e−subproblem using (12).
Update u using (8).
Update v using (9).
End for.

References

1. Van de Linde, S. *et al.* Direct stochastic optical reconstruction microscopy with standard fluorescent probes. *Nat. protocols* 6, 991 (2011).
2. Rust, M. J., Bates, M. & Zhuang, X. Sub-diffraction-limit imaging by stochastic optical reconstruction microscopy (STORM). *Nat. methods* 3, 793 (2006).
3. Hess, S. T., Girirajan, T. P. & Mason, M. D. Ultra-high resolution imaging by fluorescence photoactivation localization microscopy. *Biophys. journal* 91, 4258–4272 (2006).
4. Betzig, E. *et al.* Imaging intracellular fluorescent proteins at nanometer resolution. *Science* 313, 1642–1645 (2006).
5. Fölling, J. *et al.* Fluorescence nanoscopy by ground-state depletion and single-molecule return. *Nat. methods* 5, 943 (2008).
6. Henriques, R. *et al.* QuickPALM: 3D real-time photoactivation nanoscopy image processing in ImageJ. *Nat. methods* 7, 339 (2010).
7. Sharonov, A. & Hochstrasser, R. M. Wide-field subdiffraction imaging by accumulated binding of diffusing probes. *Proc. Natl. Acad. Sci.* 103, 18911–18916 (2006).
8. Dong, B. *et al.* Super-resolution spectroscopic microscopy via photon localization. *Nat. communications* 7, 12290 (2016).
9. Huang, B., Wang, W., Bates, M. & Zhuang, X. Three-dimensional super-resolution imaging by stochastic optical reconstruction microscopy. *Science* 319, 810–813 (2008).
10. Jones, S. A., Shim, S., He, J. & Zhuang, X. Fast, three-dimensional super-resolution imaging of live cells. *Nat. methods* 8, 499 (2011).
11. Aristov, A., Lelandais, B., Rensen, E. & Zimmer, C. ZOLA-3D allows flexible 3D localization microscopy over an adjustable axial range. *Nat. Commun.* 9, 2409 (2018).
12. Song, K.-H., Zhang, Y., Wang, G., Sun, C. & Zhang, H. F. Three-dimensional biplane spectroscopic single-molecule localization microscopy. *Optica* 6, 709–715 (2019).
13. Huang, B., Jones, S. A., Brandenburg, B. & Zhuang, X. Whole-cell 3D STORM reveals interactions between cellular structures with nanometer-scale resolution. *Nat. methods* 5, 1047 (2008).
14. Pavani, S. R. P. *et al.* Three-dimensional, single-molecule fluorescence imaging beyond the diffraction limit by using a double-helix point spread function. *Proc. Natl. Acad. Sci.* 106, 2995–2999 (2009).

15. Juette, M. F. *et al.* Three-dimensional sub–100 nm resolution fluorescence microscopy of thick samples. *Nat. methods* 5, 527–529 (2008).

16. Shtengel, G. *et al.* Interferometric fluorescent super-resolution microscopy resolves 3d cellular ultrastructure. *Proc. Natl. Acad. Sci.* 106, 3125–3130 (2009).

17. Jia, S., Vaughan, J. C. & Zhuang, X. Isotropic 3D super-resolution imaging with a self-bending point spread function. In *CLEO: Science and Innovations*, CTh5D–10 (Optical Society of America, 2013).

18. Munro, I. *et al.* Accelerating single molecule localization microscopy through parallel processing on a high-performance computing cluster. *J. microscopy* 273, 148–160 (2019).

19. Holden, S. J., Uphoff, S. & Kapanidis, A. N. DAOSTORM: an algorithm for high-density super-resolution microscopy. *Nat. methods* 8, 279 (2011).

20. Zhu, L., Zhang, W., Elnatan, D. & Huang, B. Faster STORM using compressed sensing. *Nat. methods* 9, 721 (2012).

21. Zhang, S., Chen, D. & Niu, H. 3D localization of high particle density images using sparse recovery. *Appl. optics* 54, 7859–7864 (2015).

22. Ovesný, M., Křížek, P., Švindrych, Z. & Hagen, G. M. High density 3D localization microscopy using sparse support recovery. *Opt. express* 22, 31263–31276 (2014).

23. Gu, L. *et al.* High-density 3D single molecular analysis based on compressed sensing. *Biophys. journal* 106, 2443–2449 (2014).

24. Wang, Y. *et al.* Blind sparse inpainting reveals cytoskeletal filaments with sub-Nyquist localization. *Optica* 4, 1277–1284, DOI: 10.1364/OPTICA.4.001277 (2017).

25. Boyd, S., Parikh, N., Chu, E., Peleato, B. & Eckstein, J. Distributed optimization and statistical learning via the alternating direction method of multipliers. *Foundations Trends Mach. learning* 3, 1–122 (2011).

26. Candes, E., Demanet, L., Donoho, D. & Ying, L. Fast discrete curvelet transforms. *Multiscale Model. & Simul.* 5, 861–899 (2006).

27. Gaire, S. K. *et al.* Accelerated 3D localization microscopy using blind sparse inpainting. In *2019 IEEE 16th International Symposium on Biomedical Imaging (ISBI 2019)*, 526–529 (IEEE, 2019).

28. Yazdanpanah, A. P. & Regentova, E. E. Compressed sensing MRI using curvelet sparsity and nonlocal total variation: Cs-nltv. *Electron. Imaging* 2017, 5–9 (2017).

29. curvelet.org. http://www.curvelet.org/index.html (2008).

30. Ovesný, M., Křížek, P., Borkovec, J., Švindrych, Z. & Hagen, G. M. ThunderSTORM: a comprehensive ImageJ plugin for PALM and STORM data analysis and super-resolution imaging. *Bioinformatics* 30, 2389–2390 (2014).

31. Schindelin, J. *et al.* Fiji: an open-source platform for biological-image analysis. *Nat. methods* 9, 676 (2012).

32. Scott, D. W. Averaged shifted histograms: effective nonparametric density estimators in several dimensions. *The Annals Stat.* 1024–1040 (1985).

33. Volume Viewer. https://imagej.nih.gov/ij/plugins/volume-viewer.html (2005).

34. Single-Molecule Localization Microscopy • Software Benchmarking. http://bigwww.epfl.ch/smlm/challenge2016/real/index.html?p=Tubulin-A647-3D.

35. Li, Y. *et al.* Real-time 3D single-molecule localization using experimental point spread functions. *Nat. methods* 15, 367 (2018).

36. Wang, Z., Simoncelli, E. P. & Bovik, A. C. Multiscale structural similarity for image quality assessment. In *The Thrity-Seventh Asilomar Conference on Signals, Systems & Computers, 2003*, vol. 2, 1398–1402 (IEEE, 2003).

37. Aristov, A., Lelandais, B., Rensen, E. & Zimmer, C. ZOLA-3D allows flexible 3D localization microscopy over an adjustable axial range. https://github.com/imodpasteur/ZOLA-3D (2018).

Acknowledgements

This work is supported in part by the National Science Foundation CBET-1604531, ... The authors would like to thank Biomedical Imaging Group, Ecole Polytechniqconsiderablyue Fédérale de Lausanne (EPFL), Lausanne, Switzerland, and Imaging and Modeling lab, Institut Pasteur, Paris, France for making data available online.

Author contributions statement

L.Y. conceived the idea and supervised the research. S.K.G. perform simulation, and evaluated the results, and wrote the initial draft of the manuscript. All authors interpreted the results and revised the manuscript.

Additional information

Data availability: The experimental localization data for figure 5 is available at http://bigwww.epfl.ch/smlm/challenge2016/real/index.html?p=Tubulin-A647-3D. Similarly, localization data for figure 7 is available at https://github.com/imodpasteur/ZOLA-3D.

Competing interests: The authors declare no competing financial interests.

Description of Additional Supplementary Files

File Name: Supplementary Movie 1

Description: This movie shows an animated view of the simulated 3D super-resolution image shown in Figure 2 (c) using 10,000 frames of simulated localization data. The ViSP software was used to create the animated 3D visualization[1].

File Name: Supplementary Movie 2

Description: This movie shows an animated 3D projection of the super-resolution image shown in Figure 2 (a-c) along the y-axis using 1,000 frames, blind sparse inpainting reconstruction, and 10,000 frames of the simulated 3D image.

Supplementary references:

1. El Beheiry, M. & Dahan, M. ViSP: representing single-particle localizations in three dimensions. *Nat. Methods* **10**, 689–690 (2013).